Computational Issues in Analysis and Design of Chemical-Laser Flow-Fields

A Final Report Submitted to the
Air Force Office of Scientific Research

Principal Investigator:

W. M. Eppard
AeroSoft, Inc.
1872 Pratt Drive, Ste. 1275
Blacksburg, VA 24060
(540) 557-1900
(540) 557-1919 FAX
eppard@aerosft.com

and

E. M. Cliff
Interdisciplinary Center for Applied Mathematics
Virginia Tech
Blacksburg, VA 24061

20000804 208

REPORT DOCUMENTATION PAGE

AFRL-SR-BL-TR-00-0334

Public reporting burden for this collection of information is estimated to average 1 hour per response, and maintaining the data needed, and completing and reviewing the collection of information. Se information, including suggestions for reducing this burden, to Washington Headquarters Services, Di 1204, Arlington, VA 22202-4302, and to the Office of Management and Budget, Paperwork Reduction

1. AGENCY USE ONLY *(Leave blank)*	2. REPORT DATE	3. REPORT TYPE AND DATES COVERED
	May 8, 2000	Final Report (15 Jun 99 to 31 Dec 99)

4. TITLE AND SUBTITLE
Computational Issues in Analysis and Design of Chemical-Laser Flow-Fields

5. FUNDING NUMBERS
F49620-99-C-0023

6. AUTHOR(S)
W. Marc Eppard and Eugene Cliff

7. PERFORMING ORGANIZATION NAME(S) AND ADDRESS(ES)
AeroSoft, Inc.
1872 Pratt Drive, Suite 1275
Blacksburg, VA 24060

8. PERFORMING ORGANIZATION REPORT NUMBER

9. SPONSORING/MONITORING AGENCY NAME(S) AND ADDRESS(ES)
AFOSR/PKC
Air Force Office of Scientific Research
801 North Randolph Street, Room 732
Arlington, VA 22203-1977

10. SPONSORING/MONITORING AGENCY REPORT NUMBER
0002AB

11. SUPPLEMENTARY NOTES
Software Data Restricted

12a. DISTRIBUTION AVAILABILITY STATEMENT
Approved for public release, distribution unlimited

12b. DISTRIBUTION CODE

13. ABSTRACT *(Maximum 200 words)*

The Phase-I COIL effort has focused on extending AeroSoft's GASP and SENSE software for COIL-laser analysis and design. Important improvements include: modifications to the species diffusion model to account for effective diffusion coefficients and pressure-driven diffusion effects, modifications to account for laser power extraction, the addition of a COIL chemistry model, and the development of a strategy for implementing a coupled flow-solver/power-extraction sensitivity analysis method. Results for test problems involving helium and iodine injection showed significant effects from the pressure-diffusion terms. Fully-coupled, power-on laser simulations exhibited an instability resulting from an uncoupling of grid points caused by the bi-linear interpolation method used to transfer data back and forth between the optics mesh and the flow-solver mesh. This problem occurred when there was a large disparity in the number of grid points for the flow-solver and optics mesh in the lasing cavity. Stable power-on results, however, could be obtained for well-matched flow-solver/optics grid systems. Future plans to implement a conservative interpolation scheme should eliminate this problem.

14. SUBJECT TERMS

15. NUMBER OF PAGES
31

16. PRICE CODE

17. SECURITY CLASSIFICATION OF REPORT	18. SECURITY CLASSIFICATION OF THIS PAGE	19. SECURITY CLASSIFICATION OF ABSTRACT	20. LIMITATION OF ABSTRACT

DTIC QUALITY INSPECTED 4

1 Introduction

Chemical lasers represent an important component in many advanced weapons systems of interest to the Air Force, *e.g.,* the airborne laser program (ABL). The chemical oxygen-iodine laser, or COIL, is a short wavelength, high-power chemical laser that operates on an atomic iodine laser transition. COIL was invented in 1977 at the Air Force Weapons Laboratory, now a part of the Air Force Research Laboratory at Kirtland Air Force Base, New Mexico. AFRL/DE continues to develop COIL technology using as a primary test apparatus the 10 kilowatt-class device called RADICL (Research and Development Iodine Chemical Laser)

Research and development programs for COIL typically employ numerical analysis techniques such as computational fluid dynamics (CFD) to provide insight into laser performance and design. A common goal shared by these programs is the need to more thoroughly understand the underlying physical processes of chemical lasers so that performance may be optimized. Enhanced CFD analysis tools can play an essential role in this regard. High-resolution CFD simulations can aid in interpreting and explaining measured data, make predictions for operating conditions beyond the test database, and provide accurate estimates of laser power output. Beyond predicting the performance of a given laser configuration, new design tools are required to aid scientists in tuning, scaling and shaping a practical system. With these needs in mind, AeroSoft's Phase-I research and development program has focused on the following three goals:

1. **To develop accurate and efficient CFD analysis tools for modeling COIL lasers.**
   State-of-the-art CFD methods will be extended to include new capabilities and physical models important in COIL-type laser systems such as the RADICL.

2. **To develop high-level software tools tailored for the design and optimization of COIL lasers.**
   The continuous sensitivity equation method (CSEM) for CFD-based design will be extended to include new capabilities and physical models important in COIL-type laser systems.

3. **To develop a framework for coupling discipline-specific sensitivity analyses.**
   Work specific to this contract will lead to new sensitivity-analysis tools for the coupled fluid-dynamic/power-extraction systems in COIL-laser designs.

The Phase-I COIL effort has focused on extending AeroSoft's $\mathcal{GASP}$ and $\mathcal{SENSE}$ software for COIL lasers. $\mathcal{GASP}$ is a multi-zone, upwind, characteristic-based code, which solves the integral form of the Reynolds-Averaged Navier-Stokes equations. $\mathcal{GASP}$ models the fluid continuum with a finite number of control volumes and incorporates general thermo-chemistry modeling with an extensive thermo-chemical database. The latest version, $\mathcal{GASP}$ v4, has more efficient time-integration schemes including implicit treatment of zonal boundaries. $\mathcal{GASP}$ v4 uses a distributed-memory parallel architecture in order to exploit a wide variety of platforms. These schemes greatly improve the efficiency of the code, reducing the amount of time needed to perform a computation. AeroSoft's $\mathcal{SENSE}$ software is based on the continuous sensitivity equation method and provides flow-field sensitivities to a wide array of flow and geometric design variables. $\mathcal{SENSE}$ is available as a commercial package and has been used in a variety of applications of aerospace interest [3, 4].

The modeling effort during Phase-I included modifications to $\mathcal{GASP}$'s thermo-chemical database, improvements to the species diffusion model, and modifications to account for laser power extraction. The thermo-chemical database manager has been modified to allow chemical species to be present at multiple energy states, *e.g.*, $I\left({}^2P_{1/2}\right)$ and $I\left({}^2P_{3/2}\right)$; a feature characteristic of COIL chemistry models. A 20-reaction, 10-species COIL chemistry model has also been added to the thermo-chemical database. The species diffusion model in $\mathcal{GASP}$ v4 has been extended to account for effective diffusion coefficients as well as the pressure-driven diffusion effects that are important in COIL lasers. The enhanced diffusion model has also been added to $\mathcal{SENSE}$. The diffusion models in both $\mathcal{GASP}$ v4 and $\mathcal{SENSE}$ have been tested for injection problems involving helium and iodine at conditions similar to the RADICL injector. The results show significant effects from the pressure-diffusion terms. Software modifications have also been made to $\mathcal{GASP}$ v4 to account for laser power extraction in the optical cavity. This task involved adding lasing source terms to the iodine species continuity equations and the global energy equation, implementing a geometric optics resonator model, and including interpolation methods between the flow-solver grid and the optics grid. Power-off simulations have been performed for the RADICL test configuration to test the new chemistry model. Fully-coupled, power-on laser simulations exhibited an instability resulting from an uncoupling of grid points caused by the the bi-linear interpolation method used to transfer data back and forth between the optics and flow-solver grids. This problem occurred when there was a large disparity in grid-point density between the flow-solver and optics grids in the lasing cavity. Stable power-on results, however, could be obtained for well-matched flow-solver/optics grid systems. Future plans to implement a conservative interpolation scheme should eliminate this problem. Phase-I work in the area of coupled design has focused on defining a strategy for coupling $\mathcal{SENSE}$ with a power-extraction sensitivity analysis based on the geometric optics resonator model.

2 Modifications to the Thermo-Chemical Database

The COIL laser operates on the ${}^2(P_{1/2}) \rightarrow {}^2(P_{3/2})$ transition between the spin orbit components of atomic iodine. This transition is "pumped" through energy transfer from the excited $O_2(^1\Delta)$ state of molecular oxygen. Continuous wave operation is achieved by injecting molecular iodine into a primary flow containing the excited states, $O_2(^1\Delta)$ and $O_2(^1\Sigma)$, and the ground state, $O_2(^3\Sigma)$, of molecular oxygen. Once the molecular iodine has been injected into the flow, energy pooling processes involving the excited states of oxygen result in the dissociation of molecular iodine, I_2, into atoms. This is followed by rapid energy transfer and the establishment of a population inversion in atomic iodine according to the "pumping" reaction

$$I + O_2(^1\Delta) \rightarrow I^* + O_2(^3\Sigma)\,, \tag{1}$$

and the various competing mechanisms that work to reduce I^*. Note that in Eq (1) I and I^* denote the ${}^2(P_{3/2})$ and ${}^2(P_{1/2})$ states of atomic iodine respectively. During the lasing process, it is the excited I^* state of iodine that is stimulated to emit photons, while the energy in this system is stored in the $O_2(^1\Delta)$ state. Because of the relatively large concentration of $O_2(^1\Delta)$, each iodine atom can be repumped and cycled many times before leaving the lasing cavity.

During this Phase-I effort the COIL chemistry model in Table 1 has been added to $\mathcal{GASP}$'s thermo-chemical database. The I_2 dissociation mechanism consists of the two separate reaction paths described by reactions 7 and 11. Reactions 1, 2, 8, 9, and $12-14$ affect the I_2 dissociation process through the production (or destruction) of $O_2(^1\Sigma)$ and I_2^*. Reaction 15 is the pumping reaction, and reactions $3-6$, 10, and $16-20$ work to deactivate the system by reducing either $O_2(^1\Delta)$ or I^*. The forward reaction rates for each reaction are constant and given in Table 1. The backward rates are computed using the forward rates and the equilibrium constant which is determine through the LeRC curve fits and the minimization of Gibb's free energy.

As indicated in the above discussion, the COIL chemistry mechanism is used (in part) to model transitions in the internal energy states of the oxygen and iodine species. As a result, the various energy states of a given molecule or atom must be represented as a separate species in the thermo-chemical database. To accommodate this feature, a tagging convention has been added to the

No.	Reaction	Mechanism	$K_f(Kg-mole, m^3, s)$
1	$O_2(^1\Delta) + O_2(^1\Delta) \rightarrow O_2(^1\Sigma) + O_2(^3\Sigma)$	I_2 Dissociation $(+\,O_2(^1\Sigma))$	4.035×10^9
2	$O_2(^1\Sigma) + H_2O \rightarrow O_2(^1\Delta) + H_2O$	I_2 Dissociation $(-\,O_2(^1\Sigma))$	9.635×10^9
3	$O_2(^1\Delta) + O_2(^3\Sigma) \rightarrow O_2(^3\Sigma) + O_2(^3\Sigma)$	Competing $(-\,O_2(^1\Delta))$	2.409×10^3
4	$O_2(^1\Delta) + H_2O \rightarrow O_2(^3\Sigma) + H_2O$	Competing $(-\,O_2(^1\Delta))$	9.635×10^2
5	$O_2(^1\Delta) + Cl_2 \rightarrow O_2(^3\Sigma) + Cl_2$	Competing $(-\,O_2(^1\Delta))$	4.818×10^0
6	$O_2(^1\Delta) + He \rightarrow O_2(^3\Sigma) + He$	Competing $(-\,O_2(^1\Delta))$	2.288×10^{10}
7	$I_2 + O_2(^1\Sigma) \rightarrow 2\,I + O_2(^3\Sigma)$	I_2 Dissociation $(+\,I)$	1.204×10^9
8	$I_2 + O_2(^1\Sigma) \rightarrow I_2 + O_2(^3\Sigma)$	I_2 Dissociation $(-\,O_2(^1\Sigma))$	6.323×10^{10}
9	$I_2 + O_2(^1\Delta) \rightarrow I_2^* + O_2(^3\Sigma)$	I_2 Dissociation $(+\,I_2^*)$	4.215×10^6
10	$I_2 + I^* \rightarrow I_2^* + I$	Competing $(-\,I^*)$	1.807×10^{11}
11	$I_2^* + O_2(^1\Delta) \rightarrow 2\,I + O_2(^3\Sigma)$	I_2 Dissociation $(+\,I)$	3.011×10^{10}
12	$I_2^* + O_2(^3\Sigma) \rightarrow I_2 + O_2(^3\Sigma)$	I_2 Dissociation $(-\,I_2^*)$	1.807×10^{11}
13	$I_2^* + H_2O \rightarrow I_2 + H_2O$	I_2 Dissociation $(-\,I_2^*)$	2.409×10^9
14	$I_2^* + He \rightarrow I_2 + He$	I_2 Dissociation $(-\,I_2^*)$	6.022×10^5
15	$I + O_2(^1\Delta) \rightarrow I^* + O_2(^3\Sigma)$	Pumping $(+\,I^*)$	6.624×10^7
16	$I + O_2(^1\Delta) \rightarrow I + O_2(^3\Sigma)$	Competing $(-\,O_2(^1\Delta))$	9.635×10^6
17	$I^* + O_2(^1\Delta) \rightarrow I + O_2(^1\Sigma)$	Competing $(-\,I^*)$	1.626×10^4
18	$I^* + O_2(^1\Delta) \rightarrow I + O_2(^1\Delta)$	Competing $(-\,I^*)$	4.697×10^{10}
19	$I^* + I \rightarrow 2I$	Competing $(-\,I^*)$	6.022×10^7
20	$I^* + H_2O \rightarrow I + H_2O$	Competing $(-\,I^*)$	2.409×10^9

Table 1: 10-species, 20-reaction COIL chemistry model

Species	Database Name
$O_2(^3\Sigma)$	`O_2`
$O_2(^1\Delta)$	`(O_2)_[sd]`
$O_2(^1\Sigma)$	`(O_2)_[ss]`
I_2	`I_2`
I_2^*	`(I_2)_[star]`
$I(^2P_{3/2})$	`I`
$I(^2P_{1/2})$	`(I)_[star]`

Table 2: Thermo-chemical database species naming convention.

thermo-chemical database manager which allows a chemical species to be present at multiple energy states. The various energy levels of oxygen and iodine have been entered into the database as shown in Table 2. Figures 1 and 2 illustrate the new naming convention as shown in the species and model windows of the database manager for the COIL mechanism.

3 Effective Diffusion Model

Pressure diffusion terms have been shown to be important in the injector region of the COIL where a 2:1 or greater pressure ratio must exist for sonic injection to be achieved. During Phase-I an effective diffusion model with pressure-gradient terms has been added to the viscous formulation in $\mathcal{GASP}$ v4. The diffusion terms appear in the species continuity equations as well as the global energy equation. The continuity equation for species s is given by

$$\frac{\partial}{\partial t}\iiint \rho_s \, dV + \oint_A (\rho_s \mathbf{V} \cdot \hat{\mathbf{n}}) \, dA = \oint_A \left(-\rho_s \vec{\mathcal{V}}_s \cdot \hat{\mathbf{n}}\right) dA + \iiint \omega_s \, dV \,. \tag{2}$$

where ρ_s is the density of species s, $\mathbf{V}$ is the velocity vector, ω_s represents the chemistry production term for species s, and $\vec{\mathcal{V}}_s$ is the diffusion velocity vector for species s. Prior to this contract the

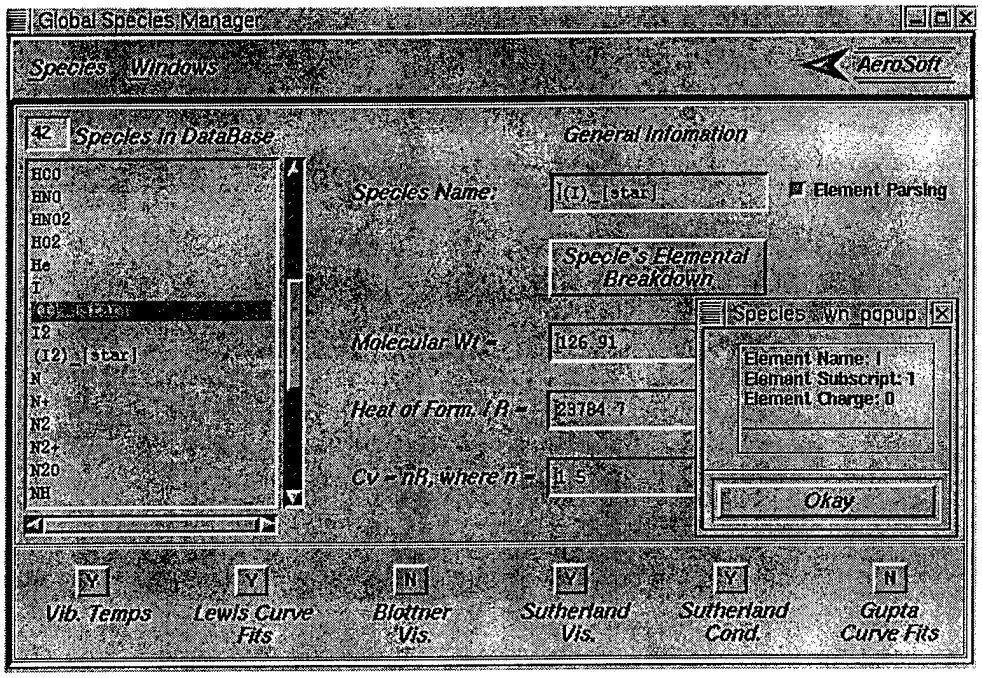

Figure 1: Species window illustrating new species naming convention and species parsing

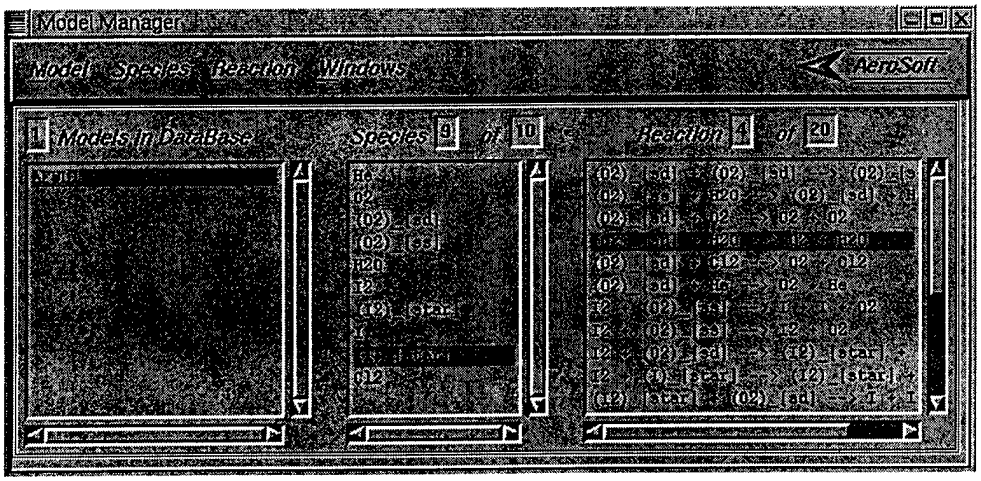

Figure 2: Model window illustrating the new COIL chemistry model

species diffusion velocity was given by Fick's law

$$\rho_s \vec{\mathcal{V}}_s = -\rho D_s \nabla(\rho_s/\rho)\,, \tag{3}$$

with a species diffusion coefficient determined using a constant Schmidt number as

$$D_s = \frac{\mu}{\rho\, Sc}\,. \tag{4}$$

The effective diffusion model represents a modeling improvement in that it accounts for individual species diffusion coefficients as well as pressure-driven diffusion effects. The effective diffusion model for species s is given by

$$\rho_s \vec{\mathcal{V}}_s = -\gamma_t\, \hat{M}_s\, D_{sm} \left[\bar{\nabla}\chi_s + \left(\chi_s - \frac{\rho_s}{\rho}\right)\frac{\bar{\nabla}p}{p}\right] + \gamma_t\, \frac{\rho_s}{\rho} \sum_{j=1}^{N} \hat{M}_j\, D_{jm} \left[\bar{\nabla}\chi_j + \left(\chi_j - \frac{\rho_j}{\rho}\right)\frac{\bar{\nabla}p}{p}\right], \tag{5}$$

where $\hat{M}_s$ is the species molecular weight, D_{sm} is the species effective diffusion coefficient, γ_t is the mixture concentration, and χ_s is the species mole fraction. Definitions for the species concentration, γ_s, the mixture concentration, and the species mole fraction are given respectively as

$$\gamma_s = \frac{\rho_s}{\hat{M}_s}\,, \qquad \gamma_t = \sum_{s=1}^{N} \gamma_s\,, \qquad \chi_s = \frac{\gamma_s}{\gamma_t}\,. \tag{6}$$

The species effective diffusion coefficients are given in terms of a mixture summation of the binary diffusion coefficients, $\mathcal{D}_{ij}$, as follows

$$D_{sm} = \frac{1-\chi_s}{\sum_{j=1, j\neq s}^{N} \chi_j/\mathcal{D}_{sj}}\,, \tag{7}$$

and satisfy the mass conservation constraint that

$$\sum_{s=1}^{N} \rho_s \vec{\mathcal{V}}_s = 0\,. \tag{8}$$

Closure of this system of equations requires relations for the binary diffusion coefficients, $\mathcal{D}_{ij}$, which have been determined by Hirschfelder [5] using appropriate collision integrals. The resulting equations are

$$\mathcal{D}_{ij} = 0.018828\, T^{3/2}\, \frac{\sqrt{\left(\frac{1}{\hat{M}_i} + \frac{1}{\hat{M}_j}\right)}}{p\, \sigma_{ij}^2 \Omega_{ij}}\,, \tag{9}$$

where

$$\sigma_{ij} = \frac{\sigma_i + \sigma_j}{2}\,, \tag{10}$$

$$\Omega_{ij} = \left[\frac{0.75571}{T^{*0.08742}} + \frac{0.68191}{T^{*0.84910}}\right], \tag{11}$$

$$T^* = \frac{T}{\epsilon_{ij}}\,, \tag{12}$$

and

$$\epsilon_{ij} = \sqrt{\epsilon_i\, \epsilon_j}\,. \tag{13}$$

Actual implementation of the effective diffusion model has been performed by separating the effects of mole-fraction gradients and pressure gradients. This feature allows the option to run with or without the pressure diffusion terms. Separating these effects in Eq (5) yields

$$\rho_s \vec{\mathcal{V}}_s^{\chi} = -\gamma_t \, \hat{M}_s \, D_{sm} \, \bar{\nabla} \chi_s + \gamma_t \, \frac{\rho_s}{\rho} \sum_{j=1}^{N} \hat{M}_j \, D_{jm} \, \bar{\nabla} \chi_j \, , \tag{14}$$

and

$$\rho_s \vec{\mathcal{V}}_s^{p} = -\gamma_t \, \hat{M}_s \, D_{sm} \left(\chi_s - \frac{\rho_s}{\rho} \right) \frac{\bar{\nabla} p}{p} + \gamma_t \, \frac{\rho_s}{\rho} \sum_{j=1}^{N} \hat{M}_j \, D_{jm} \left(\chi_j - \frac{\rho_j}{\rho} \right) \frac{\bar{\nabla} p}{p} \, , \tag{15}$$

such that

$$\rho_s \vec{\mathcal{V}}_s = \rho_s \vec{\mathcal{V}}_s^{\chi} + \rho_s \vec{\mathcal{V}}_s^{p} \, . \tag{16}$$

Also to facilitate ease of implementation, the following variables have been defined

$$\mathbf{G}_s^{\chi} \equiv \hat{M}_s \, D_{sm} \, \bar{\nabla} \chi_s \, , \tag{17}$$

and

$$\mathbf{G}_s^{p} \equiv \hat{M}_s \, D_{sm} \left(\chi_s - \frac{\rho_s}{\rho} \right) \, . \tag{18}$$

Utilizing these definitions, Eqs (14) and (15) become

$$\rho_s \vec{\mathcal{V}}_s^{\chi} = -\gamma_t \left[\mathbf{G}_s^{\chi} - \frac{\rho_s}{\rho} \sum_{j=1}^{N} \mathbf{G}_j^{\chi} \right] \, , \tag{19}$$

and

$$\rho_s \vec{\mathcal{V}}_s^{p} = -\gamma_t \left[\mathbf{G}_s^{p} - \frac{\rho_s}{\rho} \sum_{j=1}^{N} \mathbf{G}_j^{p} \right] \frac{\bar{\nabla} p}{p} \, . \tag{20}$$

The diffusion term resulting from mole-fraction gradients, Eq (19), behaves in a similar fashion to Fick's law and results in molecular diffusion away from mole-fraction gradients. The pressure diffusion term, Eq (20), results in molecular diffusion of "lighter" species away from pressure gradients and "heavier" species toward pressure gradients. To see this we consider a mixture of helium and iodine with molecular weights $\hat{M}_{He} = 4.003$ and $\hat{M}_{I_2} = 253.82$ respectively. The species densities, pressure and temperature are taken as $\rho_{He} = 0.010395 \, Kg/m^3$, $\rho_{I_2} = 0.007605 \, Kg/m^3$, $p = 9576 \, N/m^2$ and $T = 438.5 \, K$. These conditions results in mass fractions of $\rho_{He}/\rho = 0.5775$ and $\rho_{I_2}/\rho = 0.4225$ and mole fractions of $\chi_{He} = 0.988564$ and of $\chi_{I_2} = 0.011406$. Note that the term $(\chi_s - \rho_s/\rho)$ in Eq (18) will be positive for a species whose mole fraction is greater than its mass fraction, indicating a relatively "light" species. This same term will be negative for a species whose mole fraction is less than its mass fraction, indicating a relatively "heavy" species. Evaluating the terms in Eq (20) for the specified conditions yields

$$\rho_{He} \vec{\mathcal{V}}_{He}^{p} = -1.2456 \times 10^{-4} \, \frac{\bar{\nabla} p}{p} \, , \tag{21}$$

and

$$\rho_{I_2} \vec{\mathcal{V}}_{I_2}^{p} = +1.2456 \times 10^{-4} \, \frac{\bar{\nabla} p}{p} \, . \tag{22}$$

These results show that the lighter helium molecules diffuse in a direction opposite the pressure-gradient vector, while the heavier iodine molecules diffuse in the same direction as the pressure-gradient vector. The net effect is for light and heavy particles to tend to separate in regions of large pressure gradients.

3.1 Helium-Iodine Injection into an Infinite Chamber

As a first test problem for the new diffusion model, we considered the two-dimensional, supersonic injection of helium and iodine into an infinite chamber. Figure 3(a) shows the 81×161 computational mesh used for this case. The injector face extends from $y = 0.0\,m$ to $y = \pm 0.0005\,m$ with flow entering the domain from left to right. Solid chamber walls extend above and below the injector face. Grid points are clustered in the horizontal direction near the wall and injector face and in the vertical direction near the injector side walls. The jet Mach number was $M = 1.3$, the temperature was $T = 288\,K$, and the pressure was $p = 28728\,N/m^2$. The species densities were $\rho_{He} = 0.047480\,Kg/m^3$ and $\rho_{I_2} = 0.034737\,Kg/m^3$. Initial conditions in the chamber consisted of pure helium at Mach number of $M = 0.01$, a temperature of $T = 300\,K$, and a pressure of $p = 9576\,N/m^2$. The initial species density for helium was $\rho_{He} = 0.015368\,Kg/m^3$. The jet conditions were imposed using a split-flux free-stream boundary condition and the chamber wall was treated using a no-slip wall boundary condition. All other boundaries were treated using first-order extrapolation from the interior.

Figures 3(b), 3(c), and 3(d) show the resulting Mach number contours partially superimposed with streamtraces, pressure contours, and iodine mass fraction contours. Figures 3(b) and 3(c) indicate that the helium-iodine mixture undergoes a strong expansion as it leaves the injector, resulting in the lower pressures and higher Mach numbers shown by the contours plots. The very strong pressure gradients near the injector side walls, *i.e.*, $y = \pm 0.0005\,m$, result in large pressure-diffusion effects which work to separate the helium from the iodine. This can be seen in Fig 3(d), where the iodine concentrations in the near-wall region are essentially zero. Comparison of the streamlines in Fig 3(b) and the iodine mass fraction contours in Fig 3(d) indicate that the diffusion process occurs in a direction transverse to the mean flow velocity. Figure 4 shows the normalized pressure profile and helium and iodine mass-fraction profiles for the vertical, $i = 10$ grid line. This grid line is very close in proximity to the injector face and chamber walls. The normalized pressure profile shows a large pressure gradient at $y = +.0005\,m$ near the injector side wall. The iodine mass fraction profile shows a maxima in the high pressure-gradient region, while the helium mass fraction profile shows a minima. These results are consistent with the pressure-diffusion effects previously described. As helium molecules encounter the pressure gradient they tend to diffuse in the $+y$ direction away from the pressure gradient, resulting in a minima. Iodine molecules tend to diffuse in the $-y$ direction toward the pressure gradient resulting in the observed maxima.

3.2 Transverse Helium-Iodine Injection

As a second test problem we considered the two-dimensional, transverse injection of helium and iodine into a pure helium free stream. Figure 3(a) shows the 113×81 computational mesh used for this case. The lower surface is composed of a solid wall with the injector face located between $x = 0.0075\,m$ and $x = 0.0077\,m$. Grid points are clustered in the vertical direction near the wall and injector face and in the horizontal direction near the injector side walls. The jet conditions are identical to those in Section 3.1. The free-stream conditions are identical to the initial chamber conditions in Section 3.1, except the Mach number is $M = 0.8$ with the flow direction being left to right. As before, the jet conditions were imposed using a split-flux free-stream boundary condition and the lower wall was treated using a no-slip wall boundary condition. The subsonic inflow boundary was treated by fixing the all the flow variables except pressure to the free-stream values. The pressure at the inflow boundary was extrapolated from the interior. All other boundaries were treated using first-order extrapolation from the interior.

Figure 5(b) shows the iodine mass fraction contours for the complete domain. Figure 6(a) shows a close-up view of the pressure contours and streamtraces in the injector region. Comparison of these figures shows three distinct flow regions; the primary flow of helium which expands around the jet to supersonic speeds, the jet flow which contains regions of iodine concentrations that are slightly higher than jet free-stream values, and a recirculation region just to the right of the injector with lower than jet free-stream concentrations of iodine. The variation in iodine concentrations between the jet flow region and the recirculation region is caused by the pressure diffusion effects that tend to separate iodine and helium. Figure 6(b) shows the normalized pressure profile and iodine mass

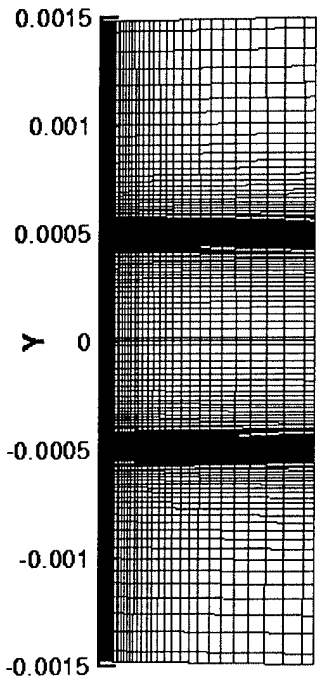

(a) Two-Dimensional, 81 × 161 grid.

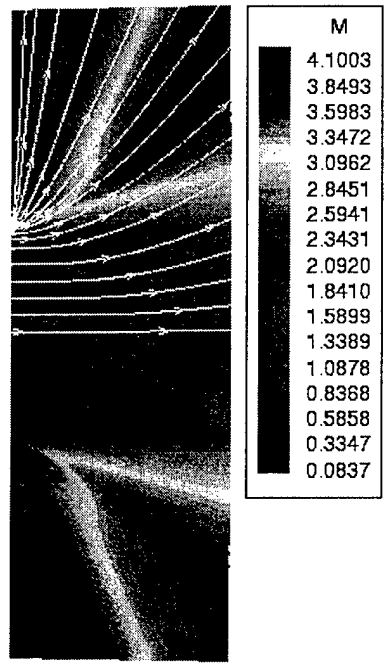

(b) Mach contours and stream-traces.

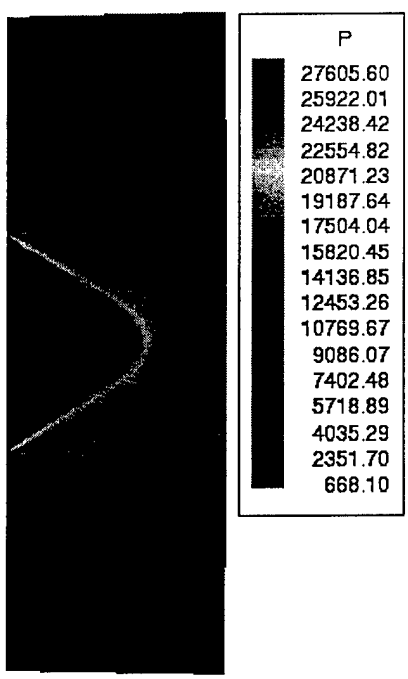

(c) Pressure contours.

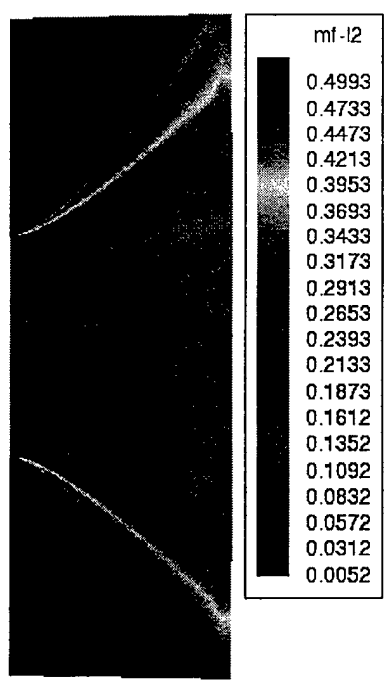

(d) Iodine mass fractions.

Figure 3: Helium-Iodine injection.

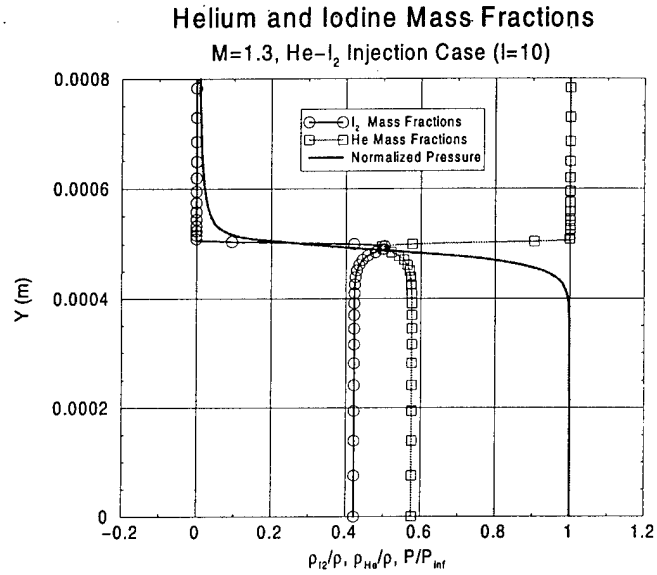

Figure 4: Helium and iodine mass fractions (station I=10)

fraction profiles for the $j = 2$ grid line in the injector region. The normalized pressure profile shows two large pressure-gradient regions in the vicinity of the injector side walls. The iodine mass fraction profile (for the effective diffusion model) shows peaks at these locations, indicating that the iodine molecules are diffusing in the direction of the pressure-gradient. This causes the jet flow to have slightly higher concentrations of iodine than expected. At the same time helium molecules are diffusing away from the pressure gradient causing the recirculation region to be composed of primarily helium. Figure 6(b) also shows the iodine mass fraction profile for a simulation using Fick's law, which has no pressure terms. In this case both the jet and recirculation region have helium and iodine concentrations consistent with the jet free-stream conditions. Figures 7(a) and 7(b) show iodine mass fraction contours in the vicinity of the injector for both the effective diffusion model and Fick's law.

4 Sensitivities for the Effective Diffusion Model

The sensitivity implementation in $\mathcal{SENSE}$ is fundamentally based on implicit-differentiation applied to the boundary-value problem describing the fluid mechanics. That is, one envisions an implicit equation

$$\mathcal{R}(\mathbf{Q}, \beta) = 0, \tag{23}$$

where $\mathbf{Q}$ denotes the distributed dependent variables (*e.g.* density, momentum, energy) and β denotes a design variable. In common terminology $\mathbf{Q}$ is known as the state and β as the design parameter. For fixed β, Eq (23) is solved for $\mathbf{Q}$. This defines a map

$$\beta \rightarrow \mathbf{Q},$$

which associates a flow solution with the specified design parameter(s). The sensitivity is the derivative of this map; it provides a linear approximation for how the flow solution will change under a small change in the design parameter. One proceeds by formally differentiating Eq (23) to produce

$$\frac{\partial \mathcal{R}}{\partial \mathbf{Q}} \frac{\partial \mathbf{Q}}{\partial \beta} + \frac{\partial \mathcal{R}}{\partial \beta} = 0. \tag{24}$$

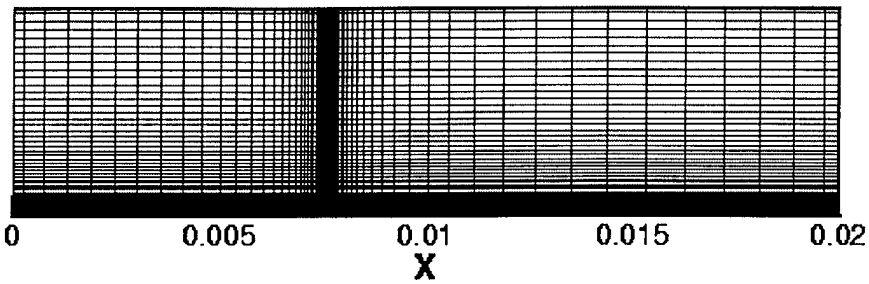

(a) 2-Dimensional, 113 × 81 grid.

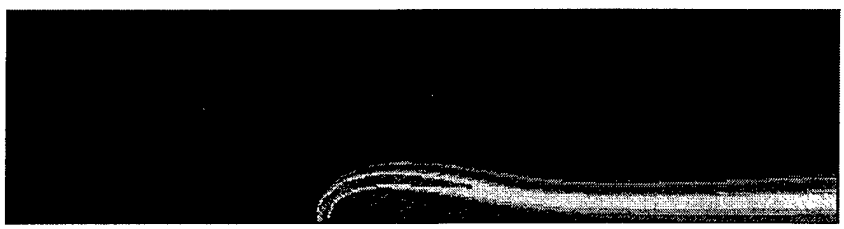

(b) Iodine mass fraction contours.

Figure 5: Helium-iodine transverse injection case.

The $\mathcal{SENSE}$ code implements a numerical approximation to Eq (24) for situations wherein $\mathcal{R}$ models Reynolds-Averaged Navier-Stokes flows with finite-rate chemistry.

The integral equations for the fluid dynamic system are written as

$$\frac{\partial}{\partial t}\iiint \mathbf{Q}\,dV + \oint_A (\mathbf{F}(\mathbf{Q})\cdot\hat{\mathbf{n}})\,dA = \oint_A (\mathbf{F}_v(\mathbf{Q})\cdot\hat{\mathbf{n}})\,dA + \iiint \mathbf{S}\,dV, \tag{25}$$

where $\mathbf{Q} = \mathbf{Q}(x, y, z, t; \beta)$ represents the vector of state variables resulting from conservation of mass, momentum and energy. The surface integrals represent the inviscid and viscous fluxes ($\mathbf{F}$ and $\mathbf{F}_v$). Changes in chemical composition are governed by the species production terms in the source term $\mathbf{S}$. Formal differentiation of Eq (25) with respect to the generic design parameter, β, results in the sensitivity equations. These equations are linear in the sensitivities. Presented in integral form, they are

$$\frac{\partial}{\partial t}\iiint \mathbf{Q}'\,dV + \oint_A (\mathbf{F}'(\mathbf{Q})\cdot\hat{\mathbf{n}})\,dA = \oint_A (\mathbf{F}'_v(\mathbf{Q})\cdot\hat{\mathbf{n}})\,dA + \iiint \mathbf{S}'\,dV, \tag{26}$$

where $\mathbf{Q}'$ is the flow sensitivity, *i.e.*, $\partial\mathbf{Q}/\partial\beta$. The inviscid and viscous flux sensitivities, $\mathbf{F}'$ and $\mathbf{F}'_v$, and the source term sensitivity, $\mathbf{S}'$, are formally given as

$$\mathbf{F}' = \frac{\partial\mathbf{F}}{\partial\mathbf{Q}}\frac{\partial\mathbf{Q}}{\partial\beta}, \quad \mathbf{F}'_v = \frac{\partial\mathbf{F}_v}{\partial\mathbf{Q}}\frac{\partial\mathbf{Q}}{\partial\beta}, \quad \mathbf{S}' = \frac{\partial\mathbf{S}}{\partial\mathbf{Q}}\frac{\partial\mathbf{Q}}{\partial\beta}. \tag{27}$$

$\mathcal{SENSE}$ solves Eq (26) using an upwind characteristic-based formulation.

As a first step toward tailoring $\mathcal{SENSE}$ for COIL-laser applications, AeroSoft has extended the viscous sensitivity formulation to include the effective diffusion model. This task required modifying the species diffusive flux sensitivity terms which are given as

$$\mathbf{F}'_v = -\frac{\partial}{\partial\beta}\left(\rho_s\,\vec{\mathcal{V}}_s\cdot\mathbf{n}\right), \tag{28}$$

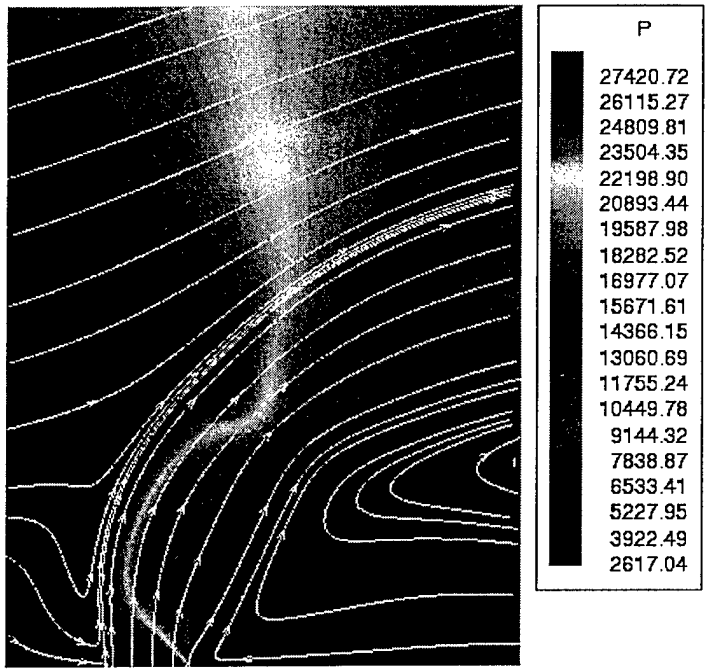

(a) Pressure contours and streamtraces.

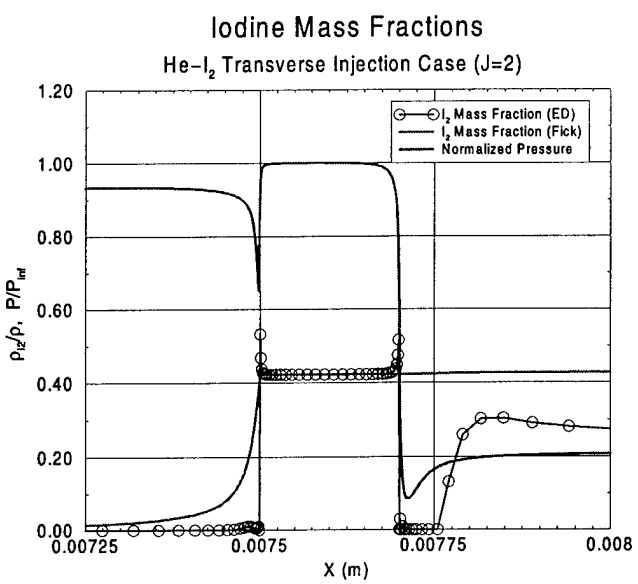

(b) Normalized pressure and iodine mass fractions.

Figure 6: Helium-iodine transverse injection case (close-up of injector).

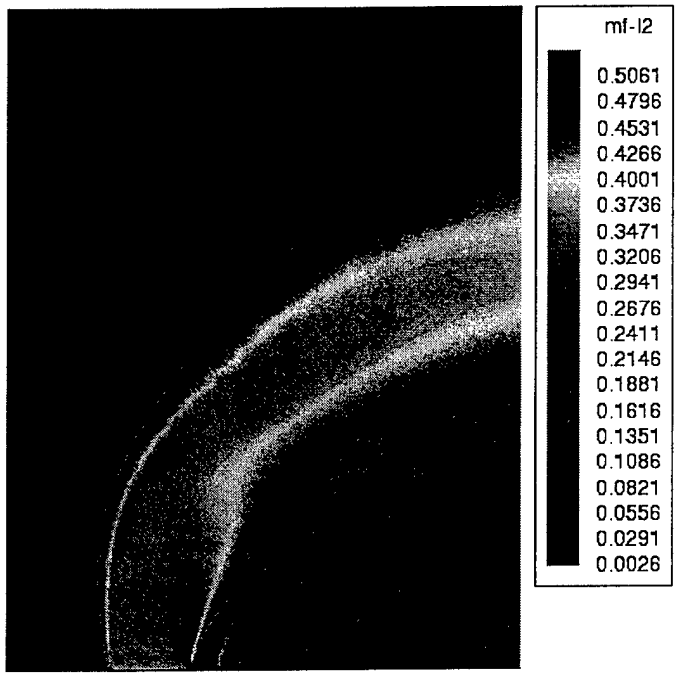

(a) Iodine mass fractions for effective diffusion model.

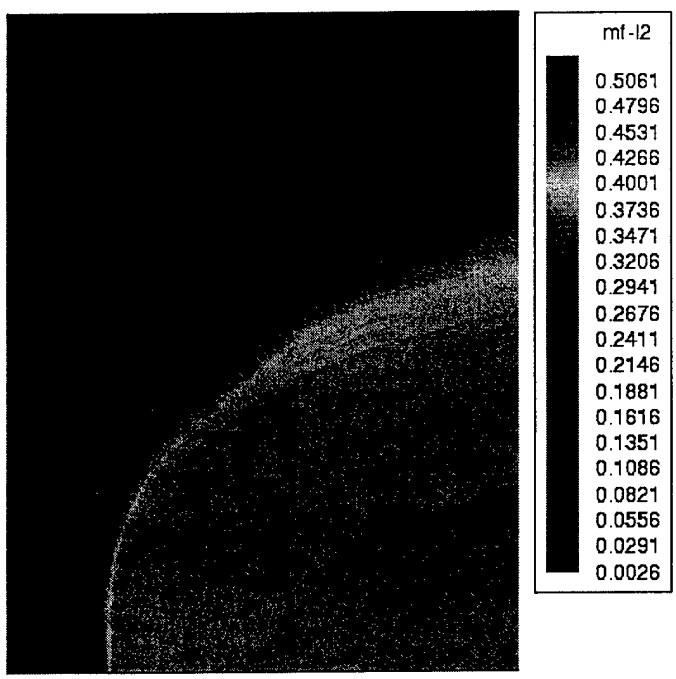

(b) Iodine mass fractions for Fick's law.

Figure 7: Helium-iodine transverse injection case (close-up of injector).

where the diffusion velocity is determined by Eqs (16) (19) and (20). The sensitivity formulation proceeds by formally differentiating Eqs (19) and (20) with respect to the design variable, yielding

$$\left(\rho_s \vec{\mathcal{V}}_s^{\chi}\right)' = -\gamma_t' \left[\mathbf{G}_s^{\chi} - \frac{\rho_s}{\rho}\sum_{j=1}^{N}\mathbf{G}_j^{\chi}\right] - \gamma_t \left[\mathbf{G}_s^{\chi\prime} - \frac{1}{\rho}\left(\rho_s' - \frac{\rho_s}{\rho}\rho'\right)\sum_{j=1}^{N}\mathbf{G}_j^{\chi} - \frac{\rho_s}{\rho}\rho'\sum_{j=1}^{N}\mathbf{G}_j^{\chi\prime}\right], \quad (29)$$

and

$$\left(\rho_s \vec{\mathcal{V}}_s^{p}\right)' = -\gamma_t' \left[\mathbf{G}_s^{p} - \frac{\rho_s}{\rho}\sum_{j=1}^{N}\mathbf{G}_j^{p}\right]\frac{\bar{\nabla}p}{p} - \gamma_t \left[\mathbf{G}_s^{p\prime} - \frac{1}{\rho}\left(\rho_s' - \frac{\rho_s}{\rho}\rho'\right)\sum_{j=1}^{N}\mathbf{G}_j^{p} - \frac{\rho_s}{\rho}\rho'\sum_{j=1}^{N}\mathbf{G}_j^{p\prime}\right]\frac{\bar{\nabla}p}{p}$$
$$-\gamma_t \left[\mathbf{G}_s^{p} - \frac{\rho_s}{\rho}\sum_{j=1}^{N}\mathbf{G}_j^{p}\right]\left(-\frac{\bar{\nabla}p}{p^2}p' + \frac{\bar{\nabla}p'}{p}\right), \quad (30)$$

where

$$\left(\rho_s \vec{\mathcal{V}}_s\right)' = \left(\rho_s \vec{\mathcal{V}}_s^{\chi}\right)' + \left(\rho_s \vec{\mathcal{V}}_s^{p}\right)'. \quad (31)$$

The individual sensitivity terms for the species concentration, the mixture concentration, and the species mole fraction are given as

$$\gamma_s' = \frac{\rho_s'}{\hat{M}_s}, \qquad \gamma_t' = \sum_{s=1}^{N}\gamma_s', \qquad \chi_s' = \frac{1}{\gamma_t}\left(\frac{\rho_s'}{\hat{M}_s} - \chi_s \cdot \gamma_t'\right). \quad (32)$$

The sensitivities of $\mathbf{G}_s^{\chi}$, $\mathbf{G}_s^{p}$, and D_{sm} are

$$\mathbf{G}_s^{\chi\prime} = \hat{M}_s D_{sm}' \bar{\nabla}\chi_s + \hat{M}_s D_{sm}\bar{\nabla}\chi_s', \quad (33)$$

$$\mathbf{G}_s^{p\prime} = \hat{M}_s D_{sm}' \left(\chi_s - \frac{\rho_s}{\rho}\right) + \hat{M}_s D_{sm}\left(\chi_s' - \frac{\rho_s'}{\rho} + \frac{\rho_s}{\rho^2}\rho'\right), \quad (34)$$

and

$$D_{sm}' = -\frac{D_{sm}}{1-\chi_s}\left[\chi_s' + D_{sm}\sum_{j=1, j\neq s}^{N}\left(\frac{\chi_j}{\mathcal{D}_{sj}} - \frac{\chi_j}{\mathcal{D}_{sj}^2}\mathcal{D}_{sj}'\right)\right]. \quad (35)$$

Finally, closure of the effective diffusion sensitivity terms is given by sensitivities of the binary diffusion coefficient

$$\mathcal{D}_{ij}' = \mathcal{D}_{ij}\left(\frac{3}{2}\frac{T'}{T} - \frac{\Omega_{ij}'}{\Omega_{ij}} - \frac{p'}{p}\right), \quad (36)$$

where

$$\Omega_{ij}' = -\left[\frac{0.06606}{T^{*1.08742}} + \frac{0.57901}{T^{*1.84910}}\right]T^{*\prime}, \quad (37)$$

and

$$T^{*\prime} = \frac{T'}{\epsilon_{ij}}. \quad (38)$$

The sensitivity relations given by Eqs (29) - (38) along with the corresponding flux-sensitivity Jacobian terms have been added to a COIL version of the $\mathcal{SENSE}$ software. A simplified helium-iodine chemistry model has also been added to the $\mathcal{SENSE}$ package.

4.1 Sensitivities of Helium-Iodine Injection

The sensitivity analysis has been applied to the helium-iodine injection case described in Section 3.1. For this case the design variable was chosen to be the jet iodine density, *i.e.*, $\beta = \rho_{I_2}{}^{Jet}$. Figures 8(a) and 8(b) show the iodine mass fractions from the $\mathcal{GASP}$ calculation and the iodine mass-fraction sensitivities, $(\rho_{I_2}/\rho)'$ from $\mathcal{SENSE}$. The iodine mass-fraction sensitivities at the injector face are imposed by the jet inflow densities and density sensitivities through the following relation

$$(\frac{\rho_{I_2}}{\rho})' = \frac{1}{\rho}\left(\rho'_{I_2} - \frac{\rho_s}{\rho}\rho'\right) . \tag{39}$$

The jet helium and mixture densities are $\rho_{I_2} = 0.034737\,Kg/m^3$ and $\rho = .082217\,Kg/m^3$. The jet helium and mixture density sensitivities are unity for this case. Under these conditions Eq (39) gives a value of $(\rho_{I_2}/\rho)' = 7.024$; the free-stream value observed in Fig 8(b). The iodine mass-fraction sensitivities are observed to have values larger than $(\rho_{I_2}/\rho)' = 7.024$ near the injector side-wall regions. This indicates that the pressure-diffusion effects become more pronounced as the iodine density in the jet increases. To see that this is plausible, we analyze the leading pressure-gradient term in Eq (15), $(\chi_{I_2} - \rho_{I_2}/\rho)$. For a 5% increase in the design variable the absolute value of this term increases from $|(\chi_{I_2} - \rho_{I_2}/\rho)| = 0.387750$ to a value of $|(\chi_{I_2} - \rho_{I_2}/\rho)| = 0.397994$ (a 2.64% increase). As a result the pressure diffusion effects should become more pronounced. Figure 9(a) shows iodine mass fraction sensitivities along the $i = 10$ grid line for both $\mathcal{SENSE}$ and a central difference approximation using $\mathcal{GASP}$ and a 5% change in design variable. The two profiles agree very well and both predict an increase in the iodine mass fraction near injector side wall. Figure 9(b) shows a close up of iodine mass fraction profiles for the baseline solution, a $\mathcal{GASP}$ solution for a 5% increase in β, and a Taylor's series projection using the baseline flow and the sensitivities from $\mathcal{SENSE}$. The projected solution agrees very well with the "exact", $\mathcal{GASP}$ solution, except for the slight lag near the start of the large pressure-gradient region.

4.2 Sensitivities of Transverse Helium-Iodine Injection

The sensitivity analysis has also been applied to the transverse helium-iodine injection case described in Section 3.2. For this case the design variable was chosen to be the jet velocity, *i.e.*, $\beta = V^{jet}$. Figure 8(a) shows the iodine mass fractions from the $\mathcal{GASP}$ calculation and Fig 8(b) shows the iodine mass-fraction and velocity-vector sensitivities. The velocity-vector sensitivities indicate an increase in the jet velocity as well as deeper penetration of the helium-iodine mixture into the primary flow. The iodine mass-fraction sensitivities also indicate that the jet flow has penetrated further into the primary flow. The region of positive (and negative) sensitivities just above (and below) the jet indicate that the jet has shifted upward. The portion of the recirculation region with low iodine mass fractions has also shifted upward, as indicated by the positive sensitivities in this area.

5 Coupling $\mathcal{GASP}$ with the Power Extraction Model

Current COIL-CFD analysis codes at AFRL/DE can be viewed as coupled fluid mechanics and laser power extraction codes. The *MINT* implementation [1] of the COIL simulation couples a pde-based model of the mechanics for compressible, viscous, chemically reacting flow with a ray-tracing model [2] for the power extraction. The $\mathcal{GASP}$ implementation described in this section follows the same construct.

5.1 Lasing Source Terms

Power extraction in the lasing cavity manifests itself in the form of source terms in the iodine species continuity equations, and in the global energy equation. The species continuity equations are affected because components at different energy states are represented as separate species. In a COIL laser, iodine in the excited, $I(^2P_{1/2})$, energy state is stimulated to emit photons (*i.e.*, stimulated emission). Upon emission of the photon, the iodine atom assumes the lower, $I\left(^2P_{3/2}\right)$, energy state. As a result,

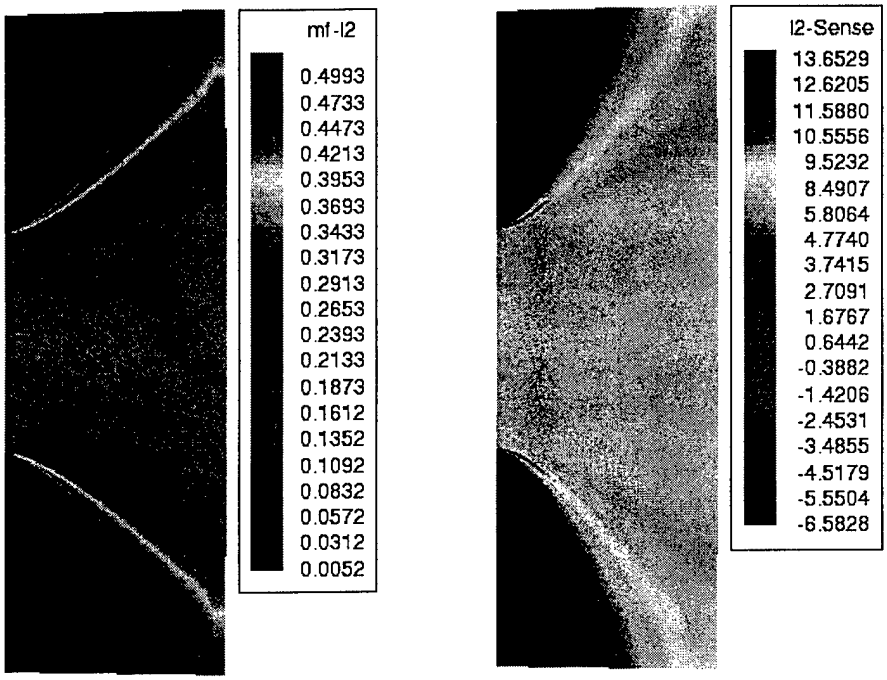

(a) Iodine mass fractions.

(b) Iodine mass fraction sensitivities.

Figure 8: Sensitivities for Helium-iodine injection.

power extraction affects the concentration of these two states. Power extraction also accounts for a net energy loss (through emission of photons) to the flow. The modified species continuity equation is given as

$$\frac{\partial}{\partial t}\iiint \rho_s \, dV + \oint_A (\rho_s \mathbf{V} \cdot \hat{\mathbf{n}}) \, dA = \oint_A \left(-\rho_s \vec{V}_s \cdot \hat{\mathbf{n}}\right) dA + \iiint \omega_s \, dV \pm \iiint \frac{\alpha \, I \, \hat{M}_s}{h\nu} \, dV \,, \tag{40}$$

where the last term on the right-hand side of Eq (40) is the power-extraction source term. The source term is composed of the gain, α, the two-way average intensity, I, the molecular weight, M_s, and the energy of a photon, $h\nu = 90956 \, J/g - mole$. The field variable, α, represents the gain and is defined as

$$\alpha = \frac{7}{12}\left(\frac{A\lambda^2}{8\pi}\right) \phi(v) \left(\hat{N}_{I^*} - \frac{1}{2}\hat{N}_I\right) , \tag{41}$$

where

$$\phi(v) = \frac{2}{\Delta v_D}\left(\frac{\ln 2}{\pi}\right)^{1/2}\left[1 - \mathrm{erf}\left\{\frac{\Delta v_L}{\Delta v_D}\sqrt{\ln 2}\right\}\right] \exp\left(\left\{\frac{\Delta v_L}{\Delta v_D}\sqrt{\ln 2}\right\}^2\right) , \tag{42}$$

and

$$\Delta v_D = \frac{2}{\lambda}\sqrt{\frac{2RT\ln 2}{m_I}} \,, \tag{43}$$

$$\Delta v_L = \frac{T_{ref}}{T} P \sum_{i=1}^{N} \alpha_s \chi_s \,. \tag{44}$$

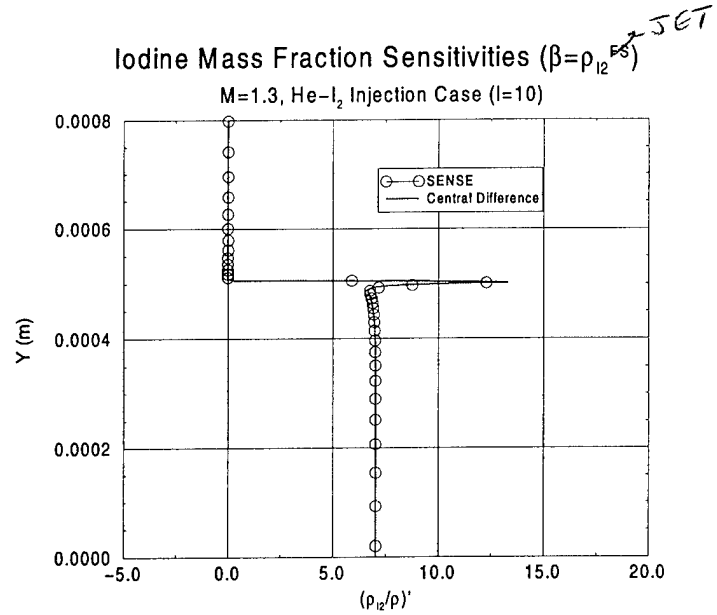

(a) Iodine mass fraction sensitivities (station I=10).

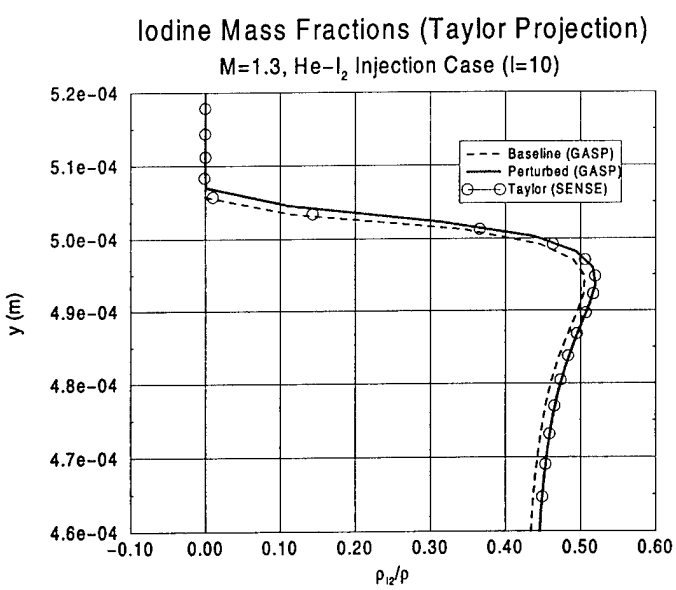

(b) Projected iodine mass fractions for 5% increase in β (Close up).

Figure 9: Sensitivities and Taylor projection for helium-iodine injection.

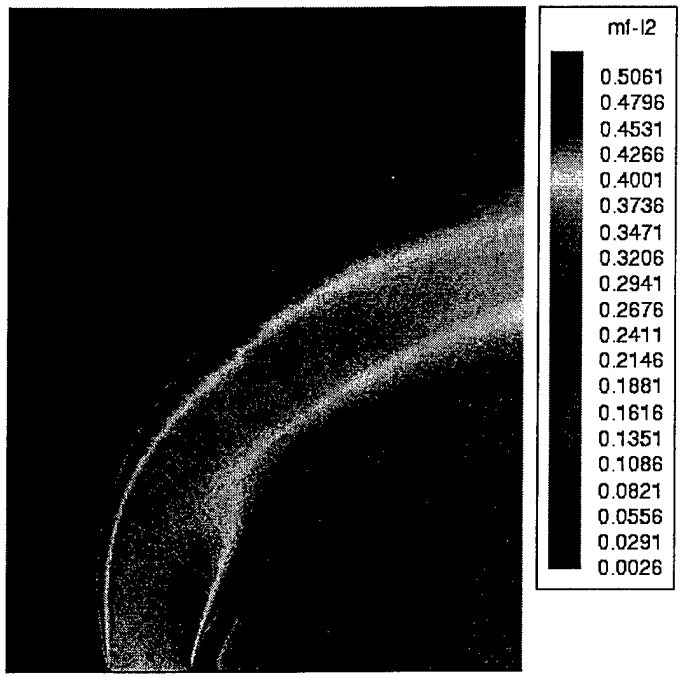

(a) Iodine mass fractions.

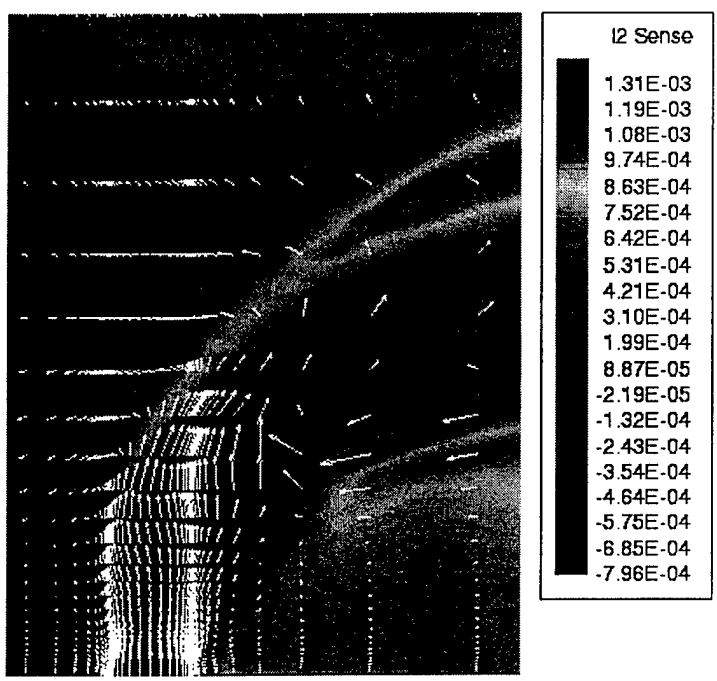

(b) Iodine mass-fraction and velocity-vector sensitivities.

Figure 10: Sensitivities for transverse helium iodine injection.

Here $\hat{N}_{I^*}$ and $\hat{N}_I$ represent number densities for the excited and ground states of atomic iodine and $\phi(v)$ is the Voight line-shape function. The constants A and λ are taken as $A = 5.0\,sec^{-1}$ and $\lambda = 1.31527 \times 10^{-4}\,cm$. The plus sign in Eq (40) is used for the ground state of iodine and the minus sign is used for the excited state. No other species in the model will have a source term contribution from the power extraction model. The global energy equation will have a similar source term, $-\alpha\, I$, to account for the energy removed from the flow.

The two-way average intensity, I, is provided as output from the optics resonator model (in this case the ray-trace model of Ref [2]), and is a function of the gain, the mirror radii and reflectivities, the geometry of the optical cavity, and various transmission and diffractive losses.

5.2 The Coupled Model

In the coupled model we have two systems, a fluid-dynamic system denoted by $\mathcal{R}_f$ and a laser power system denoted by $\mathcal{R}_p$

$$\mathcal{R}_f(u_f, u_p) = 0 \tag{45}$$

$$\mathcal{R}_p(u_f, u_p) = 0\,. \tag{46}$$

Here, the variable u_f describes the fluid-dynamic *state* and the variable u_p describes laser-power *state*. An overview of the coupled fluid-dynamic/power-extraction analysis procedure is as follows:

1. The CFD flow solver uses a pseudo-time iteration to drive the flow residual (*i.e.* $\mathcal{R}_f$) to zero. The state-variable from the laser-power extraction model, generically u_p, represents the electric field intensity, I. The intensity appears in the fluid-dynamic system in the continuity source terms for the iodine species and in the global energy equation as described in Section 5.1.

2. For a fixed intensity field I the flow iteration proceeds to reduce the flow-residual. The flow-state variable, generically u_f, includes the flow velocities, thermodynamic variables and species densities. From these known quantities we compute a gain field, α, using Eq (41). Values in the gain-field are computed pointwise from the flow-field values.

3. The gain-field is passed to the power-extraction module for the calculation of an updated intensity field. There are several steps in this linking process that arise from modeling choices. In particular, the flow simulation is based on a *unit-cell* approximation and imposes a periodic variation of the flow-variables in the direction of the optical-axis (y in [2]). Hence the gain field is averaged in the direction of the optical axis across the active region. The gain field on the flow-solver mesh is then interpolated to a two-dimensional polar mesh that is consistent with the ray-trace algorithm. At present a bi-linear interpolation method has been incorporated. The interpolated gain is then passed to the ray-trace algorithm in the array `storg(j,i)`.

4. For the given gain-field and given optical cavity geometry there is not necessarily an associated steady intensity field. Steady-state lasing occurs for the ray-trace algorithm when the round-trip gain-equals-loss condition is satisfied. Such a steady field is achieved only at gain *saturation* where gain-production and laser extraction are in equilibrium. As a result, the flow and power models must be solved simultaneously. In order to make sense of a sequential iteration procedure one must define a unique intensity field that is associated with the given gain field. The power extraction module based on [2] does this by calculating a *return intensity* and using an under-relaxation update. This process is described in more detail in Section 5.3.

5. The updated intensity field from the power extraction module is communicated back to the flow model through an array of intensities `stori(j,i)`. These intensities are then interpolated from the polar optics mesh to the flow-solver mesh where they are used to compute updated lasing source terms.

5.3 Power Extraction

The main work of the power-extraction module is done within the routine `stable.F` which was supplied by AFRL/DE. A significant code fragment is reproduced here.

```
 1000 continue
c
c     calculation of intensity on subsequent iterations, i.e., iopt = 0
c
      sdifmax = 0.0
      do 1500 i = 1,nthetal
        do 1200 j = 1,nrmax
          rod(j,i) = RABS(rmaxls(i) * (xdist - xa(j)) / distm)
          sum = storg(j,i) - scripl
          alphaq(1) = storg(j,i)
          do 1100 iq = 2,m
            alam = SQRT(1.0 + (rod(j,i) * af1(iq))**2)
            alphaq(iq) = xratio(j,iq) * (storg(iset(j,iq)-1,i) -
     1           storg(iset(j,iq),i)) + storg(iset(j,iq),i)
            sum = sum + alam * (alphaq(iq) - scripl)
 1100     continue
          s(j) = 2.0 * glength * sum
          exps = EXP(RMIN(expmin,s(j)))
c         ensure that stori(j,i) is not changed on restart
          if(ifirst .eq. 1) then
            iret(j) = inot(j,i)
          else
            iret(j) = inot(j,i) * r1r2m * exps * prodj(j)
          endif
          inot(j,i) = coninot * iret(j) + (1.0 - coninot) * inot(j,i)
          exp1 = EXP(RMIN(expmin,glength * (alphaq(1) - scripl)))
          term1 = (exp1 - 1.0) / (glength * (alphaq(1) - scripl))
          term2 = 1.0 + prodj(j) * (r1r2m * exps / (rm1 * exp1)) /
     1         (1.0 - del(j))
          stori(j,i) = inot(j,i) * term1 * term2
c
          (several lines omitted)
 1200   continue
c
          (several lines omitted)
 1500   continue
```

The `i` and `j` loops are stepped through the gain region using polar coordinates to span the (x, y) - plane in a coordinate system that is convenient for the geometry of the optical cavity. Each (`i, j`) pair labels a point on the out-coupling mirror and the calculations within the loop implement Eq (7) in [2, page 5]. A ray of initial intensity I_O leaving a point on the flat out-coupling mirror in an orthogonal direction will return (orthogonally) to the same point after $2m$ passages through the gain medium. After each passage there is a specular reflection from the opposite mirror. The return intensity is given by:

$$I_R(J) = I_O(J)(R_1 R_2)^m \exp s \prod_{p=1}^{m} (1 - \delta_p) \tag{47}$$

$$s \equiv 2L_g \sum_{p=1}^{m} (\bar{\alpha}_p - \mathcal{L})\lambda, \tag{48}$$

where R_1 and R_2 are the reflectivities of mirror 1 and 2, and $\bar{\alpha}_p$ is the average gain along the p-th ray segment. This calculation is completed in the `if` construct, that begins with the line

```
if(ifirst .eq. 1) then
```

The initial intensity field, I_O, for the next invocation of this routine is computed in the line:

```
inot(j,i) = coninot * iret(j) + (1.0 - coninot) * inot(j,i)
```

Note that this code fragment is embedded in an `i`-loop so the `i` variable does not appear explicitly in `iret()`. In the present version we have `coninot = 0.5`, so that the scheme under-relaxes the intensity field. In addition, there is a possibility of invoking the `stable.F` routine several times with the gain-field frozen at the current $\mathcal{GASP}$-supplied distribution. When the coupled system converges the *initial* and *return* intensity values will agree, so that, in effect, the relaxation calculation is identical to $I_O = I_R$, or

```
inot(j,i) = iret(j)
```

Finally, the average two-way intensity in this region of the gain field is computed from Eq (29) in [2, page 11].

$$\bar{I}_1 = \frac{I_O(J)\left[\exp\left[(\alpha(J) - \mathcal{L})L_g\right] - 1\right]}{\left[\alpha(J) - \mathcal{L}\right]L_g}\left[1 + \frac{\exp\left[-\left(\alpha(J) - \mathcal{L}\right)L_g\right]}{R_1[1 - \delta(J)]}\right]. \tag{49}$$

This calculation is (almost) implemented in the final assignment:

```
stori(j,i) = inot(j,i) * term1 * term2
```

The `stori` array is communicated back to the $\mathcal{GASP}$ flow code where it is projected onto the flow-solver grid.

5.4 Software Modifications

During Phase I, AeroSoft has performed modifications to $\mathcal{GASP}$ v4 to facilitate the power-extraction model. The new additions to $\mathcal{GASP}$ include:

1. Memory allocation for the gain and intensity fields.
2. Gain computation routine.
3. Lasing source term and Jacobian routines.
4. Parallel logic to gather the gain from zones (within the lasing cavity) on distributed processors.
5. Parallel logic to scatter the intensity to zones (within the lasing cavity) on distributed processors.
6. Routines to define the optics parameters and generate the polar mesh.
7. Implementation of the `stable.F` routine.
8. Interpolation routines between the flow-solver mesh and the polar optics mesh.
9. Iteration strategy for updating intensity.
10. Flow visualization capability for gain.

5.5 Fully-Coupled COIL Laser Simulations

Initial attempts to perform a fully-coupled, power-on, RADICL simulation yielded solutions with divergent lasing power. The resulting flow fields exhibited localized regions within the lasing cavity where the intensity continued to grow unbounded. It was hypothesized that this instability resulted from an "uncoupling" of grid points caused by the bi-linear interpolation method used to transfer the gain and intensity back and forth between the flow-solver mesh and the polar optics mesh. Figure 11 shows the superimposed flow-solver and polar optics meshes and will be used to illustrate the potential problems with the bi-linear interpolation method. Notice for the particular case shown here, the flow-solver mesh is very coarse relative to the optics mesh. As an example, we consider the step of transferring the intensity from the optics mesh points to the flow-solver cell center (denoted by the solid black circle). In order the interpolate the intensity from the polar mesh to the flow-solver cell center, the bi-linear scheme finds the four closest surrounding cells in the optics mesh (*i.e.,* the grey squares). These four points are then used in a bi-linear interpolation to determine the cell-center value for the intensity. However, for the case shown in Figure 11 there are two mesh points (the red triangles) inside the flow-solver cell that are never used in the interpolation procedure. The intensity at these "uncoupled" points has no influence on the flow-field. Points similar to these, in our initial RADICL simulations, coincided with locations where the intensity was allowed to grow unchecked.

In order to analyze this potential problem with the coupled model, a simplified test case was devised. In developing the grids for this case, care was taken to distribute the grid points such that a nearly one-to-one mapping between flow-solver and optics mesh points was obtained. By keeping the grid point distribution nearly the same for the two meshes, the uncoupling problem should be eliminated. The simplified test case is described in the following section.

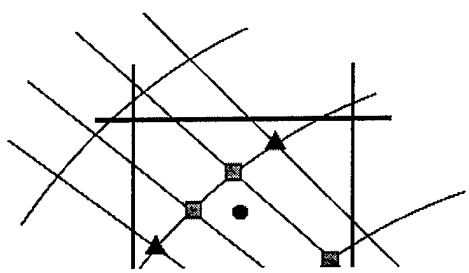

Figure 11: Bi-linear interpolation scheme.

5.5.1 Simple Test Case

Power-on simulations have been performed for a simplified flow geometry, but with flow conditions and optical parameters consistent with the RADICL laser. This test problem reduced the debugging effort and served to demonstrate the coupled processes involved in the new power-extraction model. Figure 12(a) shows the grid topology for the 151×51 flow-solver mesh and the 101×51 polar optics mesh. The number of grid points shown in this figure has been reduced to facilitate viewing. Notice that the x-direction stretching at the leading and trailing edges of the optics mesh is nearly identical to the flow solver mesh. The start of the aperture is at $x = .06\,m$ and the aperture length is $L_a = .05\,m$. The aperture height is $H_a = .028\,m$. The distance between the curved mirror and the flat out-coupling mirror is $D_m = 0.8\,m$ and the radius of curvature of the curved mirror is $r_2 = 10.0\,m$. The coefficients of reflectivity for the mirrors are $R_1 = 0.90$ and $R_2 = 0.99$ for the out-coupler and curved mirrors respectively. The gain length was taken as $L_g = 0.25\,m$. Distributed losses in the gain medium and diffractive losses at the aperture were neglected. The

Variable	High-Gain Region	Low-Gain Region
ρ_{He}	$0.00260088\,Kg/m^3$	$0.000860848\,Kg/m^3$
ρ_{O_2}	$0.00208539\,Kg/m^3$	$0.000811512\,Kg/m^3$
$\rho_{O_2(^1\Delta)}$	$0.00161352\,Kg/m^3$	$0.000831930\,Kg/m^3$
$\rho_{O_2(^3\Sigma)}$	$2.29196 \times 10^{-6}\,Kg/m^3$	$8.38014 \times 10^{-8}\,Kg/m^3$
ρ_{H_2O}	$0.000247298\,Kg/m^3$	$0.000110298\,Kg/m^3$
ρ_{I_2}	$0.000235656\,Kg/m^3$	$7.09078 \times 10^{-5}\,Kg/m^3$
$\rho_{I_2^*}$	$8.97101 \times 10^{-7}\,Kg/m^3$	$8.90463 \times 10^{-9}\,Kg/m^3$
ρ_I	$4.74918 \times 10^{-5}\,Kg/m^3$	$1.79366 \times 10^{-6}\,Kg/m^3$
ρ_{I^*}	$0.000319047\,Kg/m^3$	$4.33212 \times 10^{-6}\,Kg/m^3$
ρ_{Cl_2}	$0.00122394\,Kg/m^3$	$0.000545616\,Kg/m^3$
u	$881.8\,m/s$	$990.9\,m/s$
v	$0.0\,m/s$	$0.0\,m/s$
w	$0.0\,m/s$	$0.0\,m/s$
p	$1124.6\,N/m^2$	$1200.0\,N/m^2$

Table 3: Inflow conditions for laser test case.

inflow boundary was split into two portions; with the lower stream having a high concentration of I^* (high-gain region), and an upper stream with very little I^* and $O_2(^1\Delta)$ (low-gain region). The low-gain region was designed to account for the region of low gain observed near the upper wall in the power-off RADICL simulations. The inflow conditions for the test case were chosen from actual conditions (upstream of the lasing cavity) for the power-off RADICL simulation, and are listed in Table 3.

For this test case the uncoupling problem did not occur and the power-on solution produced a converged value for the lasing power. The solid line in Figure 13 shows the convergence history for the lasing power in this case. Figures 12(b) and 12(c) show the gain and intensity contours for this simulation. Values for the inflow gain in the high and low-gain regions are approximately $\alpha = 1.065\ 1/m$ and $\alpha = 0.00751\ 1/m$ respectively. The maximum gain occurs in the high-gain region just before the start of the aperture and has a value of $\alpha_{max} = 1.308\ 1/m$. Past the start of the aperture, the gain is dramatically reduced through interaction with the lasing source terms. The maximum intensity occurs at the aperture leading and trailing edges with a value of $I_{max} = 3.6 \times 10^9\,W/m^2$. The power output for this case converged after approximately 1000 iterations and was $P = 13.1\,KW$.

In a second test, the same case was run but with a coarsened flow-solver mesh. The coarse flow-solver mesh was obtained by sequencing five levels in both the x and y directions, yielding a 31×11 grid. The 101×51 optics mesh from the previous test above was used. The grid mismatch in this case should increase the possibility that grid-point uncoupling similar that shown in Fig 11 will occur. As expected, the lasing power for this case did not converge. The dashed line in Fig 13 shows the lasing power history for this case.

One possible fix to the uncoupling problem would be to use a conservative interpolation method. In this scheme, a pseudo-cell would be constructed around each optics grid point. The intensity at the flow-solver cell center would then be influenced by each optics cell that overlaps with the flow-solver cell. Using this method, all optics mesh points would be included in the interpolation stencil.

5.5.2 Minimum-Volume RADICL Simulation

Based on the known coupling problem with the bi-linear interpolation method, new RADICL simulations have been performed for better-matched flow-solver/optics grid systems. Figure 14(a) shows the grid topology for the $201 \times 26 \times 4$ flow-solver mesh and the 61×15 polar optics mesh. As in the previous example, the aperture length is $L_a = .05\,m$. The aperture height is $H_a = .03\,m$, the distance between the curved mirror and the flat out-coupling mirror is $D_m = 0.8\,m$ and the radius

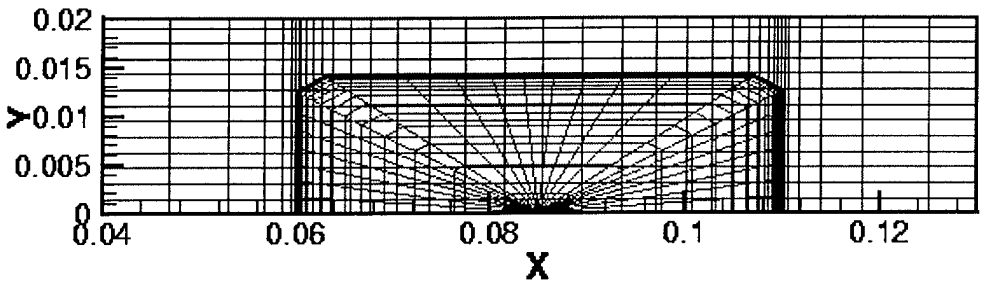

(a) Coarsened flow-solver mesh and polar optics mesh.

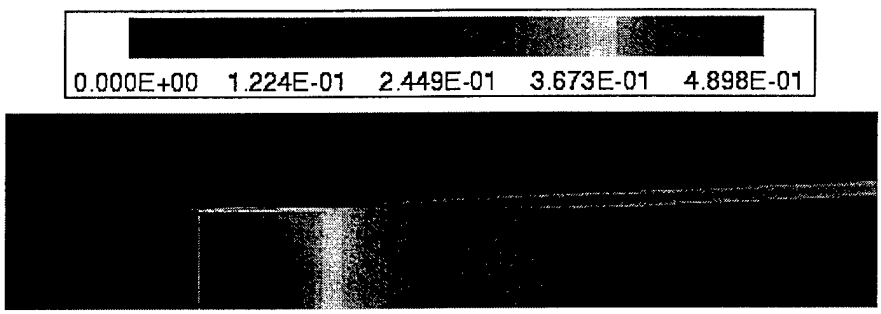

(b) Gain contours ($1/m$).

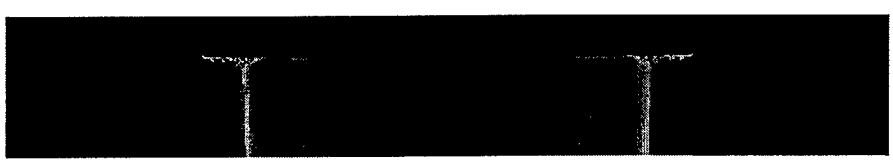

(c) Intensity contours ($Watts/m^2$).

Figure 12: Test laser configuration and results.

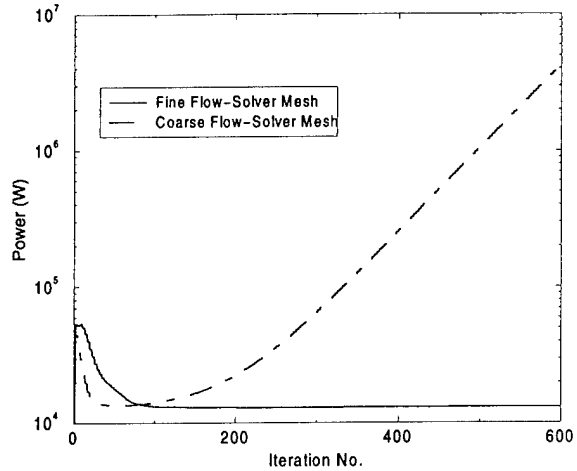

Figure 13: Lasing power vs. iteration number.

of curvature of the curved mirror is $r_2 = 10.0\,m$. The coefficients of reflectivity for the mirrors are $R_1 = 0.90$ and $R_2 = 0.99$ for the out-coupler and curved mirrors respectively. The gain length was taken as $L_g = 0.25\,m$. Distributed losses in the gain medium and diffractive losses at the aperture were neglected.

Figure 14(b) shows the gain contours for the power-off case while Figure 14(c) shows the gain contours for the power-on case. For the power-on case, the maximum gain occurs in the high-gain region just before the start of the aperture. Past the start of the aperture, the gain is dramatically reduced through interaction with the lasing source terms. The maximum intensity occurs at the aperture leading and trailing edges with a value of $I_{max} = 9.2 \times 10^8\,W/m^2$. The power output for this case was approximately $P = 8.64\,KW$. Figure 15 shows the intensity contours in the lasing cavity.

6 Coupled Sensitivity Analyses

During Phase-I the AeroSoft/ICAM team has focused on defining a strategy for coupling the flow-field sensitivity solver $\mathcal{SENSE}$ with a sensitivity analysis method for COIL power-extraction. The primary objective is to obtain flow-field and lasing sensitivities for the coupled model described in Section 5. Current COIL-CFD analysis codes at AFRL/DE can be viewed as coupled fluid mechanics and laser power extraction codes. The $\mathcal{GASP}$ implementation described in Section 5 follows this same construct, as does our initial study of the sensitivity calculations. In future efforts we will study a continuous model of the power extraction based on a paraxial wave equation [7, 6].

While it is possible to develop and implement a sensitivity-solver specifically for the COIL system we propose to study a general scheme for coupling sensitivity analyses for two distinct disciplines, here: fluid mechanics and laser power extraction. The virtue of this approach is that it leads to re-usable software, and can be carried over to other coupled systems of interest to the Air Force.

In an implicitly-coupled model we have

$$\mathcal{R}_f(u_f, u_p, \beta) = 0 \tag{50}$$

$$\mathcal{R}_p(u_f, u_p, \beta) = 0, \tag{51}$$

where the u_f variable describes the fluid *state*, the u_p variable describes laser-power *state*, and β is a scalar design variable.

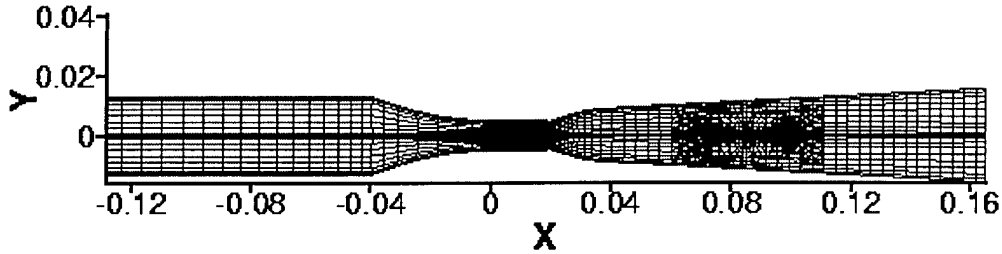

(a) $201 \times 26 \times 4$ flow-solver mesh with embedded 61×15 optics mesh.

(b) Gain contours for power-off case.

(c) Gain contours for power-on case.

Figure 14: Minimum-Volume RADICL simulation (power on and off).

The corresponding coupled sensitivity equation is described by the system

$$\begin{bmatrix} \frac{\partial \mathcal{R}_f}{\partial u_f} & \frac{\partial \mathcal{R}_f}{\partial u_p} \\ \frac{\partial \mathcal{R}_p}{\partial u_f} & \frac{\partial \mathcal{R}_p}{\partial u_p} \end{bmatrix} \cdot \begin{pmatrix} \frac{\partial u_f}{\partial \beta} \\ \frac{\partial u_p}{\partial \beta} \end{pmatrix} + \begin{pmatrix} \frac{\partial \mathcal{R}_f}{\partial \beta} \\ \frac{\partial \mathcal{R}_p}{\partial \beta} \end{pmatrix} = \begin{pmatrix} 0 \\ 0 \end{pmatrix}. \tag{52}$$

One approach to the coupled sensitivity problem builds on the existing $\mathcal{SENSE}$ software by employing a Jacobi or Gauss-Seidel iterative procedure to the coupled system (52).

An alternative formulation begins with an explicit representation of the laser field replacing (51) with

$$u_p = \mathcal{H}(u_f, \beta) \tag{53}$$

Note that the existing power-extraction module can be viewed as a method for (approximately) evaluating the function $\mathcal{H}$. If this explicit representation is substituted into (50) we obtain

$$\mathcal{R}_f(u_f, \mathcal{H}(u_f, \beta), \beta) = 0.$$

This result can, in turn, be implicitly differentiated to yield the coupled flow-sensitivity equation

$$\left[\frac{\partial \mathcal{R}_f}{\partial u_f} + \frac{\partial \mathcal{R}_f}{\partial u_p} \cdot \frac{\partial \mathcal{H}}{\partial u_f}\right] \cdot \frac{\partial u_f}{\partial \beta} + \left[\frac{\partial \mathcal{R}_f}{\partial u_p} \cdot \frac{\partial \mathcal{H}}{\partial \beta} + \frac{\partial \mathcal{R}_f}{\partial \beta}\right] = 0. \tag{54}$$

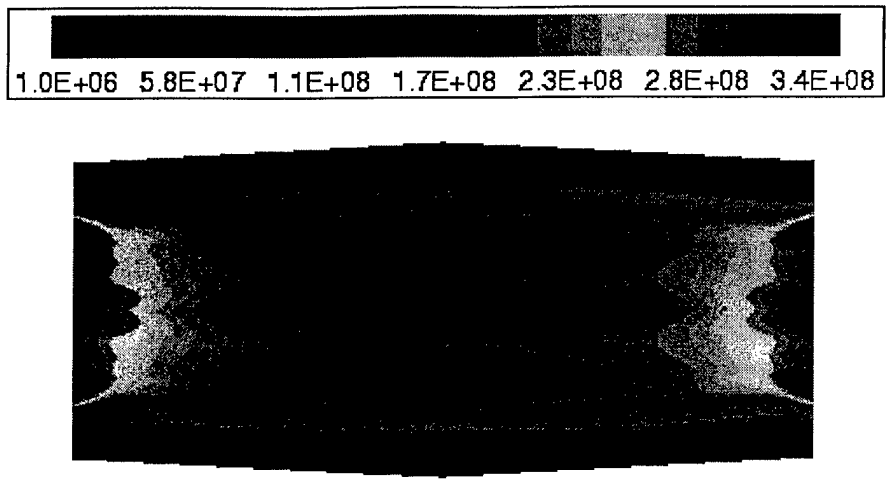

Figure 15: Minimum-Volume RADICL intensity contours (W/m^2).

6.1 Sensitivity Calculations

In Section 6 above we provided two forms for the sensitivity calculation: Eq (52) based on a general implicitly-coupled formulation; and, Eq (54) for a partially explicit formulation. The structure suggested by the `stable.F` routine is an admixture of these.

Conceptually there are several distinct intensity fields represented in `stable.F`.

1. an *initial* intensity field represented by the array `inot`,
2. a *return* intensity field represented by the array `iret`, and
3. a *two-way* intensity field represented by the array `stori`.

The purpose of the code is the evaluation of the *two-way* intensity field, which represents the coupling to the flow code. The *initial* and *return* intensities are, in a sense, internal field variables used in the calculation. At convergence of the coupled flow-intensity systems these two internal fields have the same value. Specifically, the algorithm computes a *return* intensity-field and ultimately a two-way intensity field based on the current gain-field and an *initial* intensity-field. The latter is computed by a relaxation method from the previous invocation of the routine. Thus, we suggest the abstract description

$$u_p^{n+1} = \mathcal{H}(u_f, u_p^n, \beta). \tag{55}$$

At convergence $u_p^{n+1} = u_p^n$. We compute the sensitivity at a given solution for the coupled flow-intensity fields, so that we use the semi-explicit form of Eq (51)

$$\mathcal{R}_p(u_f, u_p, \beta) = u_p - \mathcal{H}(u_f, u_p, \beta). \tag{56}$$

With this structure the coupled sensitivity Eq (52) can be written as:

$$\begin{bmatrix} \frac{\partial \mathcal{R}_f}{\partial u_f} & \frac{\partial \mathcal{R}_f}{\partial u_p} \\ -\frac{\partial \mathcal{H}}{\partial u_f} & \left[\mathcal{I}_p - \frac{\partial \mathcal{H}}{\partial u_p}\right] \end{bmatrix} \cdot \begin{pmatrix} \frac{\partial u_f}{\partial \beta} \\ \frac{\partial u_p}{\partial \beta} \end{pmatrix} = \begin{pmatrix} -\frac{\partial \mathcal{R}_f}{\partial \beta} \\ \frac{\partial \mathcal{H}}{\partial \beta} \end{pmatrix}, \tag{57}$$

where $\mathcal{I}_p$ is the identity operator on the state-space where u_p lives. The form (57) is the approach we are taking in the initial COIL sensitivity studies.

For now we assume that the design parameter of interest (generically, β) does not explicitly appear in the power-extraction module. As a practical matter this rules out cases where, for example, the geometry in the optical cavity depends on β. Mathematically, we assume that the function $\mathcal{H}$ in Eq (56) does not depend explicitly on β. Our plan is to use an iterative approach to solve the coupled linear system (57). For example, a Gauss-Seidel type implementation would be of the form

$$\left(\frac{\partial \mathcal{R}_f}{\partial u_f}\right) S_f^{n+1} = -\frac{\partial \mathcal{R}_f}{\partial \beta} - \frac{\partial \mathcal{R}_f}{\partial u_p} S_p^n \tag{58}$$

$$S_p^{n+1} = \frac{\partial \mathcal{H}}{\partial u_f} S_f^{n+1} + \frac{\partial \mathcal{H}}{\partial u_p} S_p^n, \tag{59}$$

where we have used S_f and S_p to denote the flow and laser-intensity state sensitivities, respectively. That is,

$$S_f \equiv \frac{\partial u_f}{\partial \beta}, \text{ and}$$

$$S_p \equiv \frac{\partial u_p}{\partial \beta}.$$

Equation (58) will be solved using a modification of AeroSoft's $\mathcal{SENSE}$ code. The basic flow model describes compressible, laminar, viscous, chemically reacting flow. For the COIL application an effective diffusion model has been added to account for pressure gradient effects (see Section 4). The COIL chemistry model shown in Table 1 will be directly coded into a COIL-specific version of $\mathcal{SENSE}$ in the near future.

The final feature required is a modification to include the term $\frac{\partial \mathcal{R}_f}{\partial u_p} S_p^n$. This accounts for the effect of variations of the laser intensity on the source terms in the flow equations. The term is calculated pointwise throughout the flow field using the most recently calculated intensity-sensitivity, which is communicated to the flow-sensitivity code in the same way the intensity field is communicated to the flow-solver.

The intensity-sensitivity S_p is updated as in Eq (59). The procedure for implementing this calculation is realized in a new piece of code, based on the `stable.F`. At an abstract level the dependence of the map $\mathcal{H}$ on the flow-field is naturally decomposed into two stages: a map from flow-field to gain-field; followed by a map from the gain-field to the intensity-field. In symbols

$$\mathcal{H}(u_f, u_p) = \mathcal{M}(\mathcal{N}(u_f), u_p),$$

where $\mathcal{N}$ maps the flow-field, pointwise, to the associated gain-field, and $\mathcal{M}$ maps the gain-field, intensity field pair to the associated intensity-field. The required Frechét derivative is calculated via the chain-rule

$$\frac{\partial \mathcal{H}}{\partial u_f} = \frac{\partial \mathcal{M}}{\partial u_g} \frac{\partial \mathcal{N}}{\partial u_f}.$$

The $\mathcal{N}$ map, operating pointwise, is an ordinary function of the flow-field data (see Eq 41). Flow-field sensitivity information, such as sensitivity of the various number densities to the design parameter are available from the the modified $\mathcal{SENSE}$-code. From Eq (41) and the chain-rule (again) we can explicitly calculate the gain-field sensitivity. The intermediate matrix in this chain-rule is our calculation of the term $\frac{\partial \mathcal{N}}{\partial u_f}$. As in the coupled flow-power calculation various grid systems must be reconciled. Eventually, we compute an array of gain sensitivities, say `storg_sense([],[])`. This is the representation of the sensitivity of the gain-field to changes in the parameter.

The function $\mathcal{M}$ maps the gain-field, initial intensity field to an *new* intensity-field and is implemented in the `stable.F` code. This is represented symbolically in Eq (56). Our initial implementation of the Gauss-Seidel iteration for the sensitivity calculation will follow the approach used in the coupled flow solution. Specifically, the u_p variable in Eq (55) is identified with the initial intensity field, which at convergence, agrees with the return intensity field. Equation (55) is implemented in `stable.F` in the line

```
iret(j) = inot(j,i) * r1r2m * exps * prodj(j)
```

The sensitivity of the *initial/return* intensity field will be represented on the cavity grid by a new array `inot_sense([],[])`. The implementation of the second Gauss-Seidel update, *i.e.,* Eq (59), is symbolically given by:

```
inot_sense([],[]) = inot_sense([],[]) * r1r2m * exps * prodj(j)
     + inot(j,i) * [ r1r2m * exps * prodj(j) ]_sense
```

where `[ r1r2m * exps * prodj(j) ]_sense` denotes the β-derivative of the term in brackets.

$$\frac{\partial}{\partial\beta}\left[\mathtt{r1r2m} * \mathtt{exps} * \mathtt{prodj(j)}\right]$$

Under our simplifying hypothesis, that β does not explicitly effect the cavity, the term simplifies to

$$\left[\mathtt{r1r2m} * \mathtt{prodj(j)}\right]\frac{\partial}{\partial\beta}\left[\mathtt{exps}\right]$$

In these expressions, `exps` is the exponential term

$$\exp(s),$$

where the argument s is given by Eq (47), *viz*

$$s \equiv 2L_g \sum_{p=1}^{m}(\bar{\alpha}_p - \mathcal{L})\lambda.$$

The β-parameter enters here through the gain-field, that is in the variable $\bar{\alpha}_p$ which is computed from the stored gain-field `storg`. The required expression is

$$\frac{\partial\ [\exp(s)]}{\partial\beta} = \exp(s)\sum_{p=1}^{m}\lambda_p\frac{\partial\ \bar{\alpha}_p}{\partial\beta}.$$

Since $\bar{\alpha}_p$ is an average of the gain along a particular ray through the gain-field it is a linear function of the data in the array `storg([],[])`. Its β-derivative is this same linear function of the entries in the gain-sensitivity array `storg_sense([],[])`.

The two-way intensity-field is computed from the initial intensity-field according to (49). Hence the β-derivative of the two-way intensity-field can be computed by differentiating the expression in (49). The result will involve the sensitivity of the initial intensity-field, represented by the array `inot_sense([],[])`, as well as the explicit gain-field sensitivity, represented by `storg_sense([],[])`. The resulting two-way intensity-field sensitivity will be coded in a new array (say) `stori_sense([],[])`. This is communicated back to the flow sensitivity code $\mathcal{SENSE}$ in the same way that the two-way intensity-field (`stori([],[])`) is communicated to the flow solver, $\mathcal{GASP}$.

We will modify this code so that, when an appropriate flag is set, we also calculate the derivative. For example, one fragment of the code is (new code marked by asterisks):

```
              sum = storg(j,i) - scripl
              alphaq(1) = storg(j,i)
*             if (flag_sense) then
*                sum_sense = storg_sense(j,i)
*                alphaq_sense(1) = storg_sense(j,i)
*             endif
          do 1100 iq = 2,m
            alam = SQRT(1.0 + (rod(j,i) * af1(iq))**2)
            alphaq(iq) = xratio(j,iq) * (storg(iset(j,iq)-1,i) -
     1          storg(iset(j,iq),i)) + storg(iset(j,iq),i)
```

```
            sum = sum + alam * (alphaq(iq) - scripl)
*           if (flag_sense) then
*              alphaq_sense(iq) = xratio(j,iq) * (storg_sense(iset(j,iq)-1,i) -
*    1            storg_sense(iset(j,iq),i)) + storg_sense(iset(j,iq),i)
*              sum_sense = sum_sense + alam *  alphaq_sense(iq)
*           endif
 1100     continue
```

We continue, supplying additional code as necessary to compute the array `stori_sense([],[])`, the representation of the sensitivity of the intensity-field to changes in the design parameter.

Sections 7-11 missing!

References

[1] R. C. Buggeln, S. Shamroth, A. I. Lampson, and P. G. Crowell. "Three-Dimensional (3-D) Navier-Stokes Analysis of the Mixing and Power Extraction in a Supersonic Chemical Oxygen Iodine Laser (COIL) With Transverse I_2 Injection". AIAA Paper 94-2435, 25th *Plasmadynamics and Lasers Conference*, July, 1993.

[2] P. G. Crowell. "A Stable Resonator Geometric Optics Model for Gain Saturation and Power Extraction in COIL Devices". Contract F29601-93-C-0028, CDRL A005, *Phillips Laboratory*, Februrary, 1995.

[3] A. G. Godfrey and E. M. Cliff. "Direct Calculation of Aerodynamic Force Derivatives: A Sensitivity Equation Approach". AIAA Paper 98-0393, 36th *AIAA Aerospace Sciences Meeting and Exhibit*, January 12-15, 1998.

[4] A. G. Godfrey, W. M. Eppard, and E. M. Cliff. "Using Sensitivity Equations for Chemically Reacting Flows". AIAA Paper 98-4805, 7th *AIAA/USAF/NASA/ISSMO Symposium on Multi-disciplinary Analysis and Optimization*, September 2-4, 1998.

[5] J. O. Hirschfelder, C. F. Curtiss, and R. B. Bird. **Molecular Theory of Gases and Liquid**. John Wiley and Sons, Library of Congress CCN 54-7621, 1954.

[6] A. E. Siegman. **Lasers**. University Science Books, Mill Valley, California, 1986.

[7] J. T. Verdeyen. **Laser Electronics, Third Edition**. Prentice-Hall, 1995.